Jupiter's Tropospheric Thermal Emission I: Observations and Techniques

JOSEPH HARRINGTON[1,2] AND TIMOTHY E. DOWLING

Department of Earth, Atmospheric, and Planetary Sciences, Room 54-410, Massachusetts Institute of Technology, Cambridge, Massachusetts 02139
E-mail: jh@tecate.gsfc.nasa.gov

AND

RICHARD L. BARON[2]

Institute for Astronomy, University of Hawai'i, Honolulu, Hawai'i 96822

Revision 1.2 submitted to *Icarus* 30 June 1995.
Revision 2.3 submitted to *Icarus* 18 March 1996.

---

[1]Current address:
Code 693
Goddard Space Flight Center
Greenbelt, MD 20771-0001
jh@tecate.gsfc.nasa.gov

[2]Visiting Astronomer at the Infrared Telescope Facility, which is operated by the University of Hawai'i under contract from the National Aeronautics and Space Administration.

Pages: 23 excluding figures, tables, and cover
Figures: 7
Tables: 1

Keywords: CLOUDS, Jupiter; DATA REDUCTION TECHNIQUES; EXPERIMENTAL TECHNIQUES; IMAGE PROCESSING, Jupiter; INFRARED OBSERVATIONS, Jupiter

Proposed running heads:
Left: Harrington, Dowling, and Baron
Right: Jupiter 5-µm Imaging: Data & Techniques

Address correspondence and proofs to:
Joseph Harrington
Code 693
Goddard Space Flight Center
Greenbelt, MD 20771-0001
(301) 286-9130
(301) 286-0212 fax
jh@tecate.gsfc.nasa.gov

This paper presents a new Jupiter data set and several new techniques developed for its reduction. A companion paper (J. Harrington *et al.* 1996, Submitted to *Icarus*) uses these data to study the scales of energy deposition into Jupiter's atmosphere. We observed Jupiter's tropospheric thermal emission at a wavelength of 4.9 μm (1% bandpass) with the NASA Infrared Telescope Facility (Mauna Kea, HI). The ProtoCAM 62×58-pixel infrared array camera took a total of 229 full-disk 3×3- and 4×4-image mosaics on 19 nights spanning the period 11 Jan. through 19 Apr. 1992. Resolution was typically $0''.5 - 0''.75$. We obtained full longitude coverage on six nights. This wavelength is sensitive to emission from the ∼5-bar level, near the top of the (putative) Jovian water cloud level. Clouds located higher in the atmosphere attenuate this emission. The images show atmospheric structure at all resolved spatial scales, and have a cloud optical depth range of ∼4.6. We developed image processing techniques for finding the optimal registration of images in mosaics and for locating low-contrast planetary limbs in images of planets with many high-contrast features. Both techniques are new and generally applicable, and require no human interaction.

Editor: replace ''Submitted to Icarus'' with the actual publication reference in this issue of the journal.

INTRODUCTION

In this study we image Jupiter at 4.9 μm regularly over nearly 100 days and carry out several analyses relevant to atmospheric dynamics. This paper describes our observations and the non-interactive processing system used to reduce the data. We motivate and report our dynamical results in a companion paper (Harrington *et al.* 1996).

Wavelengths near 5 μm are important to the study of Jupiter's atmosphere. At this wavelength, overlying clouds attenuate thermal emission from near the 5-bar level, deep in the troposphere (Kunde *et al.* 1982). Until recently, only raster-scanned, single-channel data have been available at these wavelengths, and even spacecraft data have disappointingly low resolution (Magalhães *et al.* 1989, 1990). The development of 2-dimensional (2D) infrared detector arrays has enabled routine imaging of the variation in cloud opacities. Unlike Jupiter's nearly uniform appearance at other thermal wavelengths (Orton *et al.* 1991), the attenuated tropospheric emission contains horizontal structure well below the limit of current resolution.

The small number of pixels in the older infrared arrays requires a sacrifice of either the spatial resolution or the coverage familiar to CCD observers; to achieve both simultaneously requires mosaicking. Because of the difficulty of aligning our 229 mosaics by hand, we developed a new algorithm that assembles mosaics without human interaction. Our procedure finds the best fit of the pieces to one another based on the content of overlapping image regions. At 5 μm, Jupiter has high-contrast features on the disk but the disk itself has very low contrast against the sky. This is unlike any planet's visible appearance. Traditional methods poorly fit the limb in our images, so we developed a new procedure for non-interactive limb identification. Our procedure is generally applicable to locating any planetary limb. Computer programs implementing the new computational techniques are available from the corresponding author.

OBSERVATIONS

We obtained 229 full-disk, 3×3- and 4×4-image mosaics of Jupiter at wavelengths near 5 μm with the ProtoCAM 62×58-pixel InSb array camera (Toomey *et al.* 1990) at the NASA Infrared Telescope Facility (IRTF) on Mauna Kea, Hawai'i. Image scale was $0\overset{''}{.}35$/pix for 3×3 mosaics and $0\overset{''}{.}27$/pix for 4×4 mosaics. Frame exposure times were 10 and 17 sec, respectively. The frame exposure time was divided into 100 summed chip readouts. Circular variable filter spectral bandpass was 1%. Except for a few images from the first nights, the order of mosaic exposures was from left to right in each row. The rows were then stepped from north to south. Times to take a full mosaic were 11–13 minutes for manual 3×3 (first two nights), 7 minutes for automatic 3×3, and 15 minutes for 4×4 mosaics. Image quality (full-width at halfmaximum of a stellar image) was typically $0\overset{''}{.}5$ – $0\overset{''}{.}75$. Table I presents a synopsis of the observations.

Thermal infrared images require several corrections in addition to those familiar to CCD observers. Significant thermal emission from the Earth's atmosphere requires that each object image be followed immediately by an image of nearby sky for later subtraction. On most nights we also took linearity, dome and sky flat field, dark current, and bias images. Linearity data are a series of images with increasing exposure times of the uniformly-emitting dewar window cover. They are used to calibrate the array pixels' nonlinear response to light. On nights with two image scales, we took flat fields at both scales.

Mosaic assembly is based on a comparison of the overlapping regions of two images. If the contents of the overlap region changes, it makes image registration more difficult, especially if the assembly is automatic. Sources of image variation included telescope pointing, image quality (due to changing atmospheric conditions and telescope focus), planetary rotation, and thermal emission from the sky. When possible, we guided on a moon of Jupiter to stabilize pointing and tracking; doing so resulted in noticeably improved images. We also focused every few hours, whenever there was a temperature change in the dome of more than a few degrees, and whenever the images began to look poor. The image quality would have benefitted from even more frequent refocus, but we could not afford the time.

TABLE I
Synopsis of Data and Observations

Date 1992	Day[a]	From UTC[b]	To UTC[b]	λ µm	# of Mosaics 3×3	4×4	Personnel[c]	Notes
11 Jan	633	10:54	15:00	4.5	2		RLB, JH	
				4.9	4			
12 Jan	634	9:54	16:23	4.9	14		RLB, JH	360°
13 Jan	635	10:41	16:34	4.9	12		JH	
25 Jan	647	11:54	16:23	4.9	11		JH	
30 Jan	652	10:12	13:00	4.65	1		RLB, TO	sep. proj.
				4.75	1			
				4.9	4			
				5.2	1			
31 Jan	653	9:42	10:52	4.9	2		RLB, TO	sep. proj.
3 Feb	656	10:54	15:25	4.9	10		JH	
9 Feb	662	11:17	16:13	4.9	10		JH	HST
10 Feb	663	8:35	16:43	4.9	21		JH	360°, HST
27 Feb	680	7:06	14:50	4.9	24		JH	360°
28 Feb	681	7:04	15:26	4.9	21	1	JH	360°
7 Mar	689	6:14	9:23	4.9	9		JH	
8 Mar	690	6:12	10:10	4.9	12		JH	
12 Mar	694	6:05	14:27	4.9	11	5	JH	360°
20 Mar	702	6:19	8:59	4.9	8		JH	
21 Mar	703	6:36	9:20	4.9	7		JH	
22 Mar	704	6:00	13:21	4.9	8	9	JH	360°
6 Apr	719	5:22	9:24	4.9		8	JH	
19 Apr	732	5:28	9:25	4.9		13	JH	

[a] Julian day $-2,448,000$.
[b] Start time of first/last mosaic imaging sequence.
[c] List of observers: RLB: Richard Baron, JH: Joseph Harrington, TO: Tobias Owen.

Notes:

360°	Night with full longitude coverage.
sep. proj.	This night's observations were for a separate project of RLB and TO.
HST	Hubble Space Telescope observed Jupiter on this night.

The key to limiting the remaining variable effects at the telescope was rapid imaging. Each mosaicking observation was a sequence of tasks that alternated telescope motions with camera exposures and image display. The 3×3 mosaic sequence took an experienced observer 11–13 minutes to do manually. ProtoCAM's software could read image display and camera commands from a file. To support mosaicking, the IRTF staff added arbitrary telescope offsets to the command file language. This eliminated the continual observer interaction during a mosaic sequence, reducing cycle time to 7 minutes and improving the mosaics.

IMAGE PROCESSING

Each step of the noninteractive data reduction procedure is an independent, general-purpose code module. Some of these are run by higher-level modules. At the highest level is a file of keyboard commands, one per final mosaic. The commands include any special processing options a given mosaic needs, enabling reproducible individual treatment of unusual images (e.g., frames out of order or nonstandard size). Reduction consisted of five phases: frame correcting, mosaicking, centering, correcting for limb darkening, and mapping.

Frames were corrected for readout amplifier bias, nonlinear response, bad pixels, sensitivity variations (flat field), thermal emission from the sky, and orientation.

An IRTF program corrected for readout amplifier bias and pixel response linearity. We used the program's linearity correction factors to create bad pixel lists for each night with good linearity data. Interpolating data from surrounding good pixels was adequate correction. To make a night's flat field, we subtracted an average of dome images from an average of sky images, took the reciprocal of each pixel value, and normalized the result so the pixel average was unity. The dome-minus-sky method removes the thermal emission pattern of the telescope itself from the flat field.

We subtracted sky data from each object image to remove emission from the Earth's atmosphere. Sky data came from the two temporally nearest sky images and were interpolated to the time of the object frame on a per-pixel basis. Even with sky frame interpolation, the residual sky levels in the images do not match sufficiently well for mosaicking, so we adjusted the level in each image by adding or subtracting a constant value. These values are such that the overlapping sky regions of two adjacent images contain the same total flux after adjustment. Since the planet occupies the center mosaic piece(s), only the edge pieces can receive this adjustment. Further, the edge piece adjustments may not sum to zero. Even distribution of the discrepancy around the mosaic edge and an interpolated shift for the central images significantly improved the resulting mosaics.

An image assembly program then constructed mosaics from the error-corrected pieces, and a fitting program located the planetary limb in the resulting images. These new programs are described in the next two sections. We did not take planetary rotation into account when assembling the mosaics. This is the major source of the small shifts at some edges in the final mosaic. Jupiter rotated 7.9° during manual 3×3 mosaics, 4.2° during automatically-taken 3×3 mosaics, and 9.1° during 4×4 mosaics. We only used data within about 60° of the sub-earth point, and that portion of a given latitude crossed no more than two mosaic rows, giving us horizontal uncertainties of 2.3°, 1.4°, and 2.6° respectively. Rather than smooth the data to make the edge discontinuities disappear (substituting unmeasured values and possibly duplicating features), we chose instead to leave them as they were and to set uncertainties appropriately in the subsequent analysis.

Most of the light in the images comes from deep in the troposphere and is subject to attenuation according to its emission angle as it leaves Jupiter's atmosphere. To correct this effect, we divide each pixel's value by $\mu^{\kappa-1}$ where μ is the emission angle cosine and κ is a fitted parameter. We find κ by plotting lines of constant latitude in mapped images at latitudes with minimal horizontal structure. The value κ=2.25 made these plots most constant across the planetary disk in a sampling of images. This method is like the standard Minnaert method described by Veverka *et al.* (1978) and Smith *et al.* (1986). We have dropped the incident angle cosine because there is minimal reflected light in these images, as demonstrated by the lack of a shadow when Io transited the disk. We attach no physical significance to this method or to the value of κ. Because of the lack of terrestrial atmospheric species absorbing significantly at

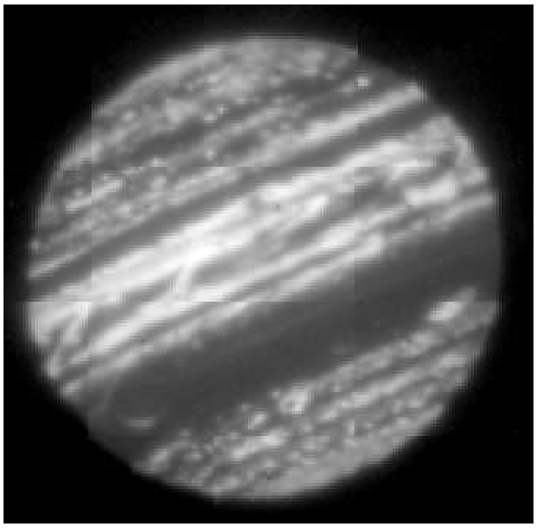

Fig. 1. Automatically-assembled 4×4-image mosaic of Jupiter taken at a wavelength of 4.9 μm on 22 March 1992 between 9:05 and 9:17 UT. This wavelength is sensitive to thermal emission from the ∼5-bar pressure level, which is attenuated by overlying clouds. The Great Red Spot is dimly visible on the left edge of the dark band in the southern hemisphere. A manually-selected low-intensity cutoff produces the sharp contrast with the sky in this logarithmically-stretched image. We have not smoothed the image or applied pixel interpolation to soften the edges of constituent pieces.

this wavelength, we did not find it necessary to compensate for terrestrial atmospheric extinction. Finally, we used a mapping program developed by T. Satoh (Goddard Space Flight Center) to create a planetographic equidistant cylindrical projection of each mosaic, and assembled sections of these to make composite maps of the planet on each observing night (see Fig. 2 and Fig. 2 of Harrington *et al.* 1996; the latter appears without overplotted quantities). As with the mosaics, we have not blended the edges to remove the small shifts in intensity at the borders of adjacent map sections.

The dark features in our images (see Figs. 1 and 2) correspond well to bright clouds in visible-light images. Images at most other wavelengths in the 3–20-μm range show a comparatively uniform planet. The most prominent dark region is the latitude band containing the Great Red Spot (GRS), which is itself only barely visible. The dark zone's width and lack of structure indicate the near-total absorption or scattering of light from below; multiply-scattered light emerging through the clouds puts the observed light level slightly higher than that of the sky. In contrast, the brightest parts of the images are always small and peaked. The lack of wide regions of uniform brightness indicates that there is cloud structure on the entire planetary disk and that there may be no completely clear regions. This means we can measure only relative cloud optical thicknesses, and it prevents a direct probe of thermal variation in the 5-bar source region. The brightest pixels on the planet have intensities over 100 times that of the dimmest, for a cloud optical depth of at least 4.6 (assuming the clouds are colder than the deep emitting region). This is a lower bound because much of the light in the dimmest regions is thought to be multiply scattered through the clouds. The mean optical depth at each latitude and the zonal wind profile of Limaye (1986) are plotted on Fig. 2 for comparison to the data.

AUTOMATIC MOSAIC ASSEMBLY

Because of the large number of mosaics and the assembly complications noted below, we developed a routine that finds the best compromise registrations of the images in a mosaic. Placing the pieces of a mosaic consists of two conceptual steps: registering

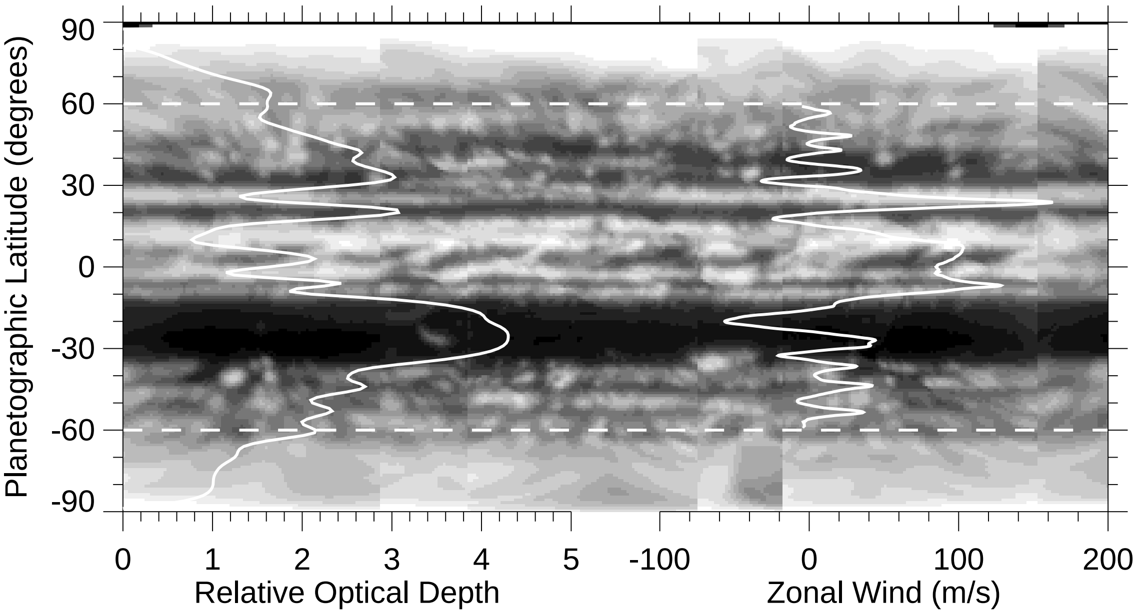

Fig. 2. Relative zonal mean optical depth (left) and Limaye (1986) zonal wind profile (right) superposed on the composite map of 22 March 1992. The optical depth plot for other nights is nearly identical. Optical depths are relative to the brightest pixel equatorward of 60° latitude (data outside this region suffer in map projection). Regional darkening such as that between -15° and -35° has been observed at other latitudes in different years, when this region has been bright.

adjacent pieces and reconciling any disagreement that results. There are several ways to choose the relative placement of two adjacent pieces in a mosaic:

1. Use knowledge of camera pointing, regardless of image content.
2. Align point-like image features (fiducial points) that appear in the overlap regions of a pair of neighboring images. Multiple fiducial points can yield subpixel registration accuracy.
3. Generate fiducial points from resolved features with a fitting algorithm. Fitting models to stars is common, as is by-eye matching.
4. Use a correlation algorithm that evaluates the overlapping portion of the two images for different candidate registrations, and chooses the best candidate.

Mosaics in two dimensions have more overlap information than needed to place all the pieces (see Fig. 3). The overlaps of adjacent pieces of an $m \times n$ mosaic provide $2mn - m - n$ relative position vectors, but we only need $mn - 1$ vectors. The vectors from real images taken in sequence may disagree slightly among themselves, but there are several ways to reconcile such differences. These include:

1. Discard enough information to make the problem go away.
2. Arbitrarily spread the disagreement among the pieces.

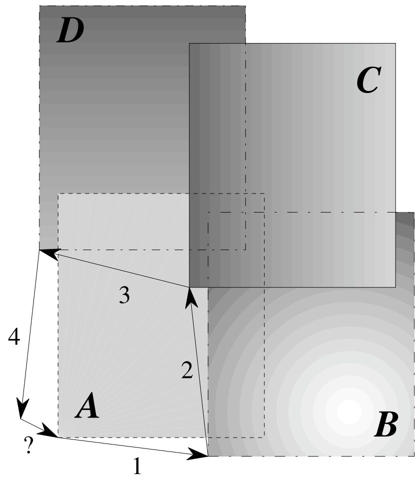

Fig. 3. This 2×2 mosaic has four (non-corner) overlaps. Each overlap determines a relative displacement vector (labeled 1–4). However, the placement of three pieces with respect to the fourth completely determines the layout of the mosaic, and requires only three vectors. The four vectors, determined by image content that can change slightly between images, may not sum to zero, leaving a small residual (labeled with a question mark). How to spread this discrepancy among the piece placements is best determined by image content.

3. Find the best fit of all the pieces, compromising based on image content.

As with most real data, many factors complicated the assembly of our mosaics. Telescope pointing was not accurate to within the point-spread function, in part due to 120–240″ beam switches to take sky images. Registration was thus necessarily by image content. Fiducial points are rare in the overlaps. Since the point-spread function was often not steady, the planet rotated up to 9.1° during one mosaic, and atmospheric features are rarely point-like near Jupiter's equator, features on the planet often changed slightly between one image and the next. This caused disagreement in the overlap information and eliminated fitting models to derive fiducial points, leaving only correlation techniques. The 3,180 image overlaps in the data set made by-eye registration impractical, but simply discarding some position information made poor mosaics. These combined problems motivated the development of an automatic mosaic assembly algorithm and a program that implements it. The program is called "jiggle."

The jiggle program consists of several independent code modules written in ANSI C. The program reads IRAF (Tody 1986) images from disk files, and can be called from IRAF or directly from the command line. The image I/O functions are especially simple to allow the integration of other image formats.

The steps in the algorithm are:

1. Define a correlation function that produces a scalar value representing the quality of a candidate registration of one image with another. See Eq. 1 and the following discussion.

2. Generate correlation images from all edge overlaps using the correlation function. Each pixel in a correlation image corresponds to one possible registration of two images. The pixel's value is the value of the correlation function for that registration. See Figs. 4 and 5.

3. Define a mosaic evaluation function. This function, given a set of mosaic piece locations in the final image, uses the correlation images to generate a single value that represents the quality of the mosaic. By convention, low values are

good. The evaluation function must have knowledge of the shape and size of the pieces so that it can select the right pixel in each correlation function.

4. Use a function minimizer to find the lowest value of the mosaic evaluation function and hence the optimal locations of all the mosaic pieces.

Correlation images are familiar from Fourier analysis (Bracewell 1986). They are a graphical representation of the quality of different registrations of two images. Figure 4 shows how pixels in correlation images map to different image registrations, and defines several of the mathematical symbols used below. Figure 5 shows some of the correlations used in the jiggle program.

Consider images $\boldsymbol{A}$ and $\boldsymbol{B}$, with dimensions $K \times L$ and $P \times Q$ pixels respectively. They are registered such that their respective rows and columns are parallel, and such that pixels $\boldsymbol{B}_{PQ}$ and $\boldsymbol{A}_{ij}$ coincide. The width and height of the overlap region are $w = \min(i, K) - \max(0, i - P)$ and $h = \min(j, L) - \max(0, j - Q)$. The image sections $\boldsymbol{a}$ and $\boldsymbol{b}$ define a secondary coordinate system whose origin in each image is the lower, left corner of the overlap region in that image. The pixel $\boldsymbol{a}_{rs} = \boldsymbol{A}_{\max(0,i-P)+r,\max(0,j-Q)+s}$ and pixel $\boldsymbol{b}_{rs} = \boldsymbol{B}_{\max(0,P-i)+r,\max(0,Q-j)+s}$.

The jiggle program's four correlations are based on the signal-to-noise ratio, least squares, and the cross correlation product rule (two methods). Below, we refer to the difference between two corresponding pixels in a candidate registration as the

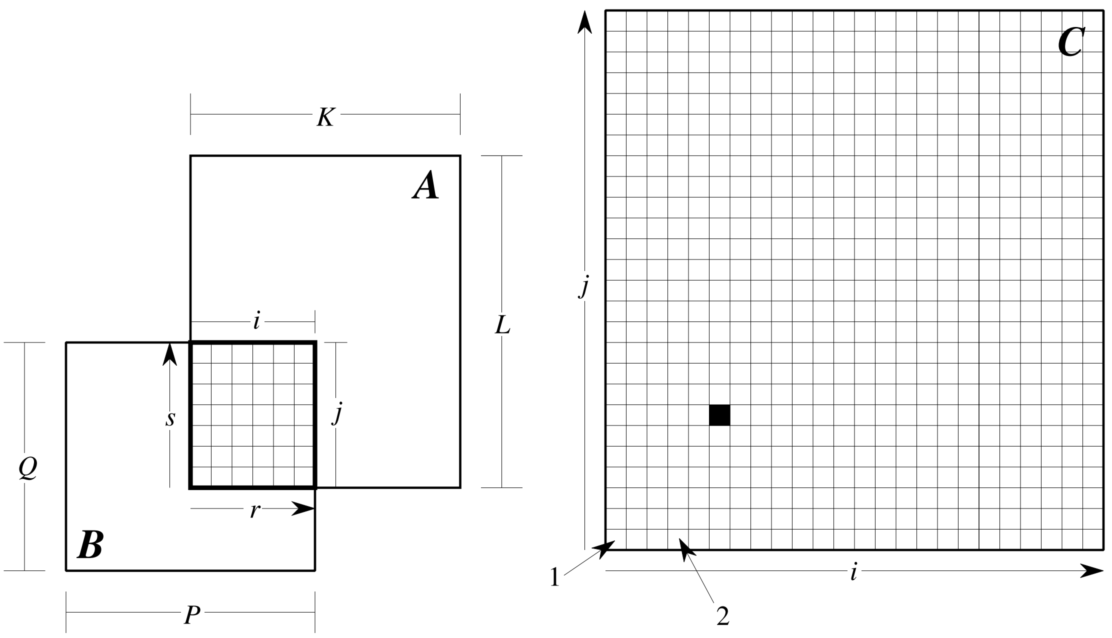

Fig. 4. Correlation image schematic. Each location in the correlation image, $\boldsymbol{C}$, represents a unique registration, or overlap, of data images $\boldsymbol{A}$ and $\boldsymbol{B}$. The correlation image has indices i and j. The value of pixel $\boldsymbol{C}_{ij}$ is that of the correlation function applied to the overlapping parts of $\boldsymbol{A}$ and $\boldsymbol{B}$. For notational simplicity, image sections $\boldsymbol{a}$ and $\boldsymbol{b}$ (not labeled), with indices r and s, refer to the indicated portions of images $\boldsymbol{A}$ and $\boldsymbol{B}$, respectively. The dark pixel in image $\boldsymbol{C}$ represents the overlap of $\boldsymbol{A}$ and $\boldsymbol{B}$ shown here. The pixel labeled 1 represents a registration such that the lowest, leftmost pixel of $\boldsymbol{A}$ and the highest, rightmost pixel of $\boldsymbol{B}$ overlap each other. Pixel 2 is the overlap of the first 4 pixels in the bottom row of $\boldsymbol{A}$ and the last 4 pixels in the top row of $\boldsymbol{B}$. The center of the correlation image represents the two images perfectly centered on one another, and so on. Figure 5 shows example correlation images.

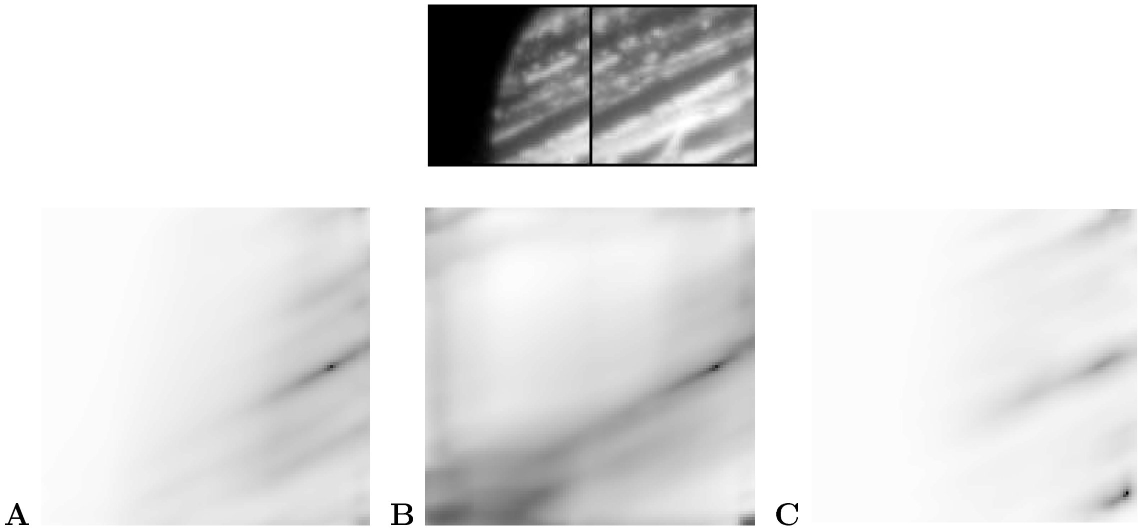

Fig. 5. These are correlation images for the overlap of two mosaic pieces (top) from Fig. 1. As described in Fig. 4, each pixel corresponds to a possible registration of the two images. Low pixel values (dark) represent a good registration. The correlation functions described in the text are: **A** squared ratio of noise to signal (best method), **B** squared noise, **C** negative of mean product (similar to cross correlation). All images have the same logarithmic stretch.

"noise" and their mean as the "signal". The methods have been inverted or negated (and renamed) to comply with the low-is-good convention. Our images (and, we suspect, most others) strongly favor the squared noise-to-signal ratio,

$$\boldsymbol{C}_{ij} = \frac{1}{wh} \sum_{s=1}^{h} \sum_{r=1}^{w} \left(\frac{\boldsymbol{b}_{rs} - \boldsymbol{a}_{rs}}{\frac{\boldsymbol{b}_{rs} + \boldsymbol{a}_{rs}}{2}} \right)^2 . \tag{1}$$

The program also offers the squared noise, which sums over $(\boldsymbol{b}_{rs} - \boldsymbol{a}_{rs})^2$; the negative mean product, with sum $-\boldsymbol{b}_{rs}\boldsymbol{a}_{rs}$; and negative total product, which is the same as the previous method but does not normalize the sum.

The eye recognizes the correct alignment of the top two images in Fig. 5 as a left-right overlap of about 1/4 of an image, with little if any vertical shift. This overlap corresponds to the darkest region in Fig. 5A. The expected value of the difference in two measurements of a bright source is higher than that value for a dim source because of Poisson noise. Taking the ratio of the noise to the signal scales a given pixel's contribution to the correlation function according to the brightness of the source at that location, and eliminates the major source of false lows in the squared noise correlation (Fig. 5B).

Astronomers most commonly use the product-based cross correlation. This method is an application of the (periodic) 2D Fourier transform (Bracewell 1986), which treats images toroidally, wrapping both left-right and top-bottom. Clearly this is undesirable. When using the cross correlation, one typically must add a constant to the images so that the mean value is zero, to avoid a tendency toward central alignment, and then must embed the data in a larger, zero-valued image to eliminate the effect of the periodic boundary condition.

The main advantage to the cross correlation is the high calculation speed associated with the fast Fourier transform algorithm (see Press *et al.* 1992). In mosaicking one can generally place a limit on how far the pieces may shift from an initial guess, reducing the calculation for brute-force methods significantly. Eliminating the transform, as our product correlations do, rids us of the periodic boundary. The negative mean product is for unaltered images and the negative total product is for images processed as above. Product correlations have some problems: Note the strong false match in the lower-right corner of Fig. 5C, which arises from the overlap of two bright regions with differing patterns.

Next we define a mosaic evaluation function. Its parameters are the vector positions of all the pieces in the mosaic except one. Scaling, rotation and other geometric adjustments that might apply as free parameters would increase this number (and complicate the correlations). The jiggle program offers a single evaluation function that returns the sum of the appropriate pixel values, one from each correlation image. Different evaluation functions might choose to emphasize certain overlaps more than others. For example, the pieces of our 4×4 Jupiter mosaics contain only a small amount of planet in each corner image. Values from the corresponding overlaps could be given less weight. Since the locations requested by the minimizer in the final step may not be integers, the evaluation function must employ an interpolator. The jiggle program uses a simple bilinear routine, but the code allows for the substitution of any interpolator.

Finally, we use a function minimizer to explore the $2(mn - 1)$-dimensional space represented by the evaluation function. This is more efficient than generating a value for each point in the evaluation space and searching for the minimal value, even for very restricted movement of mosaic pieces. The jiggle program uses the downhill simplex method (Press *et al.* 1992), though others can easily be added. Our implementation is original and improves on that presented by Press *et al.* The program then returns the corresponding optimal offsets, which other programs use to assemble the mosaic (see Fig. 1).

The jiggle program incorporates several efficiency enhancements and several more could be made. First, it only computes enough of each correlation image to include sensible offsets from the nominal positions. Other offsets are assigned large values in the correlation images so that the minimizer avoids them. Restricting the offsets reduced the time to generate correlations for our images by over a factor of 100. Second, the correlation functions are evaluated in a quadruply-nested loop. The mathematical functions are performed in line (without an explicit function call) since they are simple and function call overhead might otherwise dominate the run time on older compilers and CPU architectures. Unimplemented enhancement ideas include recording the results of each mosaic evaluation computation and re-using the values if the minimizer refers to the same point twice. Similarly, one could calculate and store correlation values only as needed, rather than doing everything within a given region. Finally, one could distinguish object from sky data by ignoring pixels whose values are outside given limits, and only use object pixels for the correlations. This would ensure that the correlation reflected only matching object features and not, for example, matching detector bias patterns in low-signal images.

Other image processing tasks may be intertwined with mosaicking, requiring an iterative approach. One example is "derotating" a planet that turned significantly during the mosaic exposures. Derotating involves a map transformation based on the size and location of the planet in the final image. It is important to select the proper order in which to do these tasks.

AUTOMATICALLY CENTERING THERMAL JUPITER IMAGES

Accurate limb identification is critical to mapping and limb-darkening corrections. Jupiter's appearance at 5 μm differs from that in visible light and this fools some limb-fitting methods. In the infrared image of Fig. 1, the brightest features have $\sim$100 times the intensity of the dim regions. Atmospheric "seeing" scatters light from bright limb features and distorts the apparent limb and surrounding scattered light pattern significantly. In the linearly-stretched visible-light image of Fig. 6, the brightest pixels have only $\sim$3.5 times the intensity of the dimmest pixels on the disk (away from the terminator) and there are no hot spots on the limb. The major contrast in the infrared image is between the bright features and anything else, whereas in the visible-light image it is between the disk and the background. The distorted infrared limb fools the most obvious limb-finding methods, and the

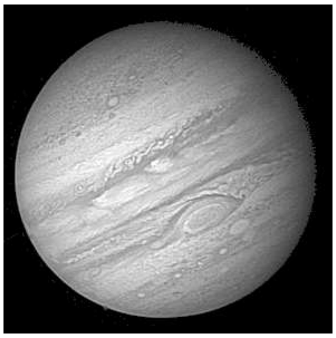

Fig. 6. Visible-light Voyager image of Jupiter. Our 4.9-μm images of Jupiter (see Fig. 1) are very different from this image. Some of the cloud belts in our images are almost as dark as the scattered light in the sky next to bright areas on the limb. Identifying the limb within the resolution limits imposed by image quality and pixel size can be challenging for computational limb-identification methods developed for visible-light images. Our new method finds the limb in 4.9-μm images and also does well at other wavelengths.

high level of activity on the disk is troublesome to others. We have developed a new limb identification method for this wavelength that should handle almost any other as well.

The new method is conceptually simple:

1. Create a slightly "fuzzed" image by convolving the original image with a one-pixel-wide Gaussian.

2. Subtract this image from the original, and set pixels with values outside reasonable limits for the limb to zero. This is similar to a truncated gradient image: both the background and the hottest areas have values at or near zero, and areas where the signal rises steeply have high values. The limb stands out as a narrow feature on much of the planet. The remaining features are fairly

randomly distributed.

3. Fuzz the image a second time with a 2-pixel-wide Gaussian. This both eliminates noise and makes the limb wider and hence easier to locate. Fig. 7 shows the intermediate and final images.

4. Define a function that returns minus the mean of pixel values on rotated ellipses in images. Since the limb consists of positive (rising signal) pixels, this function is a low-is-good quality indicator for candidate sets of high-valued pixels arrayed in an ellipse.

5. Starting with the approximate parameters for Jupiter's limb, use a function minimizer to explore the space of ellipse quality in the image. For Jupiter, good constraints include not allowing the eccentricity and orientation to vary, and not allowing the semimajor axis to vary by more than a few percent. This avoids locating the GRS instead of the limb.

After centering with the new method, a video sequence of the images did not show the rapid shifts that a sequence of images aligned with other methods showed. The "limbctr" program implements this procedure, using the bilinear image interpolator and function minimizer of the previous section, and a new quality function that evaluates rotated ellipses in image data.

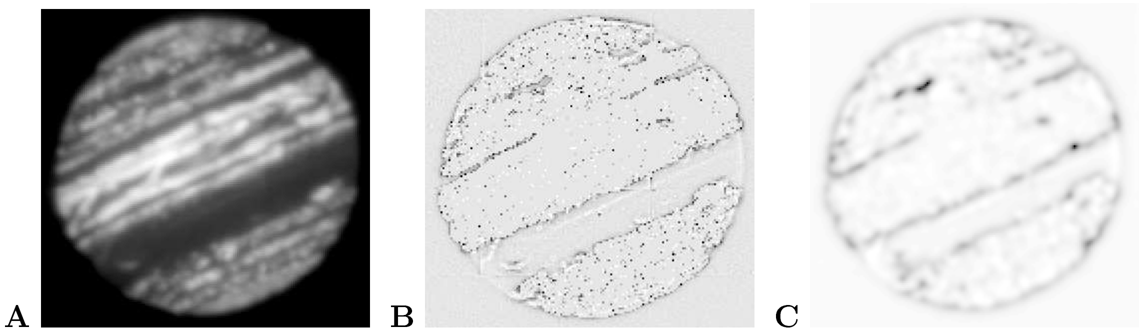

Fig. 7. Enhancing the limb in a 5-µm Jupiter image. The original image is Fig. 1. **A** The same image after convolution with a 1-pixel-wide Gaussian filter. **B** The difference between the original image and **A**, with extreme-valued pixels set to zero. **C** The final image after convolution with a 2-pixel-wide Gaussian filter. The limb now stands out as a smooth, coherent feature, wide enough not to be missed by the ellipse fit.

CONCLUSIONS

The 5-µm wavelength region reveals a deeper view of Jupiter's atmosphere than data at most other wavelengths short of the radio. However, small detector size, thermal emission from the sky, and a new planetary appearance combine to require the new observation and reduction methods we have described.

The automation of mosaic sequences at the telescope increased the number of images we were able to take and improved their quality. The change in thinking that enabled this was allowing the camera system to have synchronous control of (small) telescope motions. The reduced interaction virtually eliminated opportunities for human error and freed the observer for other tasks for most of the time needed to take a mosaic. The advantages of this approach were greater than just the 36% of cycle time saved. Exposure times for these observations were only 10 seconds. Manual motion between images thus required the operator's constant concentration, either moving the telescope or watching for the end of the exposure. Twelve hours of such work at an altitude of 4,200 meters is demanding and prone to mistakes. Alternating between two observers was the only way to maintain continuous manual observations with high efficiency. On the other hand, automated observing required attention only every 7 minutes. A single observer could easily handle the task.

The size of the data set, over 5,000 frames including calibration, motivated the development of an automated processing system. The benefit of this approach becomes clear when considering a change to an early stage of processing. To propagate such a change manually through the entire data set might mean many days of work and poor reproducibility. An automatic reduction procedure that can be run with a single command after each change ensures both reproducible work and the constant availability of the latest processed data, even when experimenting with many techniques at once. Also, one need not store many versions of each image; the raw data and the procedure together can produce any reduced data item upon request.

The two programs that implement the mosaic assembly and limb fitting techniques are available from the corresponding author. We provide these programs in the hope that they will save time and effort on others' projects, and that perhaps some might find the time to write distributable codes for other basic analysis tasks that are not covered well by the major image processing packages.

The detailed images of this data set make possible the wave search and power spectrum analysis described in our companion paper (Harrington *et al.* 1996). That paper also contains additional figures and descriptions of the data, as well as thoughts for future observers motivated by the needs of the analysis.

ACKNOWLEDGEMENTS

We thank the IRTF Time Allocation Committee for their generous allotment of telescope time, and G. Orton for helpful discussions. Special thanks go to IRTF Division Chief R. Joseph, Telescope Operators D. Griep, C. Kaminski, W. Golisch, and Programmers T. Denault and E. Pilger for their patience and assistance with the changes that made full automation at the telescope possible. We also thank T. Satoh for sharing his mapping software. Analysis work was funded by NASA Planetary Atmospheres grant NAGW-2956. IRAF is distributed by the National Optical Astronomy Observatories, which is operated by the Association of Universities for Research in Astronomy, Inc., under cooperative agreement with the National Science Foundation.

REFERENCES

BRACEWELL, R. N. 1986. *The Fourier Transform and Its Applications*, 2nd ed., revised. McGraw-Hill, New York.

HARRINGTON, J., T. E. DOWLING, AND R. L. BARON 1996. Jupiter's tropospheric thermal emission II: Power spectrum analysis and wave search. Submitted to *Icarus.*

Copy editor: please replace ''Submitted to Icarus'' with the actual publication reference in this issue.

KUNDE, V., R. HANEL, W. MAGUIRE, D. GAUTIER, J. P. BALUTEAU, A. MARTEN, A. CHEDIN, N. HUSSON, AND N. SCOTT 1982. The tropospheric gas composition of Jupiter's north equatorial belt (NH_3, PH_3, CH_3D, GeH_4, H_2O) and the Jovian D/H isotopic ratio. *Astrophys. J.* **263**, 443–467.

LIMAYE, S. S. 1986. Jupiter: New estimates of the mean zonal flow at the cloud level. *Icarus* **65**, 335–352.

MAGALHÃES, J. A., A. L. WEIR, B. J. CONRATH, P. J. GIERASCH, AND S. S. LEROY 1989. Slowly moving thermal features on Jupiter. *Nature* **337**, 444–447.

MAGALHÃES, J. A., A. L. WEIR, B. J. CONRATH, P. J. GIERASCH, AND S. S. LEROY 1990. Zonal motion and structure in Jupiter's upper troposphere from Voyager infrared and imaging observations. *Icarus* **88**, 39–72.

ORTON, G. S., A. J. FRIEDSON, J. CALDWELL, H. B. HAMMEL, K. H. BAINES, J. T. BERGSTRALH, T. Z. MARTIN, M. F. MALCOM, R. A. WEST, W. F. GOLISCH, D. M. GRIEP, C. D. KAMINSKI, A. T. TOKUNAGA, R. BARON, AND M. SHURE 1991. Thermal maps of Jupiter: Spatial organization and time dependence of stratospheric temperatures, 1980 to 1990. *Science* **252**, 537–542.

Press, W. H., S. A. Teukolsky, W. T. Vetterling, and B. P. Flannery 1992. *Numerical Recipes in C: The Art of Scientific Computing*, 2^{nd} ed. Cambridge University Press, pp. 408–412.

Smith, B. A., L. A. Soderblom, R. Beebe, D. Bliss, J. M. Boyce, A. Brahic, G. A. Briggs, R. H. Brown, S. A. Collins, A. F. Cook II, S. K. Croft, J. N. Cuzzi, G. E. Danielson, M. E. Davies, T. E. Dowling, D. Godfrey, C. J. Hansen, C. Harris, G. E. Hunt, A. P. Ingersoll, T. V. Johnson, R. J. Krauss, H. Masursky, D. Morrison, T. Owen, J. B. Plescia, J. B. Pollack, C. C. Porco, K. Rages, C. Sagan, E. M. Shoemaker, L. A. Sromovsky, C. Stoker, R. G. Strom, V. E. Suomi, S. P. Synnott, R. J. Terrile, P. Thomas, W. R. Thompson, and J. Veverka 1986. Voyager 2 in the Uranian system: Imaging science results. *Science* **233**, 43–64.

Tody, D. 1986. The IRAF data reduction and analysis system. In *Instrumentation in Astronomy VI* (D. L. Crawford, Ed.) Proc. SPIE, Vol. 627, p. 733.

Toomey, D. W., M. Shure, E. M. Irwin, and M. E. Ressler 1990. ProtoCAM - An innovative IR camera for astronomy. In *Instrumentation in Astronomy VII* Proc. SPIE, Vol. 1235, pp. 69–81.

Veverka, J., J. Goguen, S. Yang, and J. Elliot 1978. Scattering of light from particulate surfaces I. A laboratory assessment of multiple-scattering effects. *Icarus* **34**, 406–414.